The MODIS/ASTER airborne simulator (MASTER) — a new instrument for earth science studies

Simon J. Hook[a,*], Jeffrey J. Myers[b], Kurtis J. Thome[c], Michael Fitzgerald[b], Anne B. Kahle[a]

[a]*Mail Stop 183-501, Jet Propulsion Laboratory, California Institute of Technology, Pasadena, CA 91009, USA*
[b]*SAIC, NASA Ames Research Center, Moffett Field, CA 94035, USA*
[c]*Optical Sciences Center, University of Arizona, Tucson, AZ 85721, USA*

Abstract

The MODIS/ASTER Airborne Simulator was developed for the Advanced Spaceborne Thermal Emission and Reflection Radiometer (ASTER) and Moderate Resolution Imaging Spectroradiometer (MODIS) projects. ASTER and MODIS are both spaceborne imaging instruments on the Terra platform launched in the fall of 1999. Currently MASTER is flown on the Department of Energy (DOE) King Air Beachcraft B200 aircraft and the NASA DC-8. In order to validate the in-flight performance of the instrument, the Jet Propulsion Laboratory and the University of Arizona conducted a joint experiment in December 1998. The experiment involved overflights of the MASTER instrument at two sites at three elevations (2000, 4000, and 6000 m). The two sites: Ivanpah Playa, California, and Lake Mead, Nevada, were selected to validate the visible–shortwave infrared and thermal infrared (TIR) channels, respectively. At Ivanpah Playa, a spectrometer was used to determine the surface reflectance and a sun photometer used to obtain the optical depth. At Lake Mead contact and radiometric surface lake temperatures were measured by buoy-mounted thermistors and self-calibrating radiometers, respectively. Atmospheric profiles of temperature, pressure, and relative humidity were obtained by launching an atmospheric sounding balloon. The measured surface radiances were then propagated to the at-sensor radiance using radiative transfer models driven by the local atmospheric data. There was excellent agreement between the predicted radiance at sensor and the measured radiance at sensor at all three altitudes. The percent difference between the channels not strongly affected by the atmosphere in the visible–shortwave infrared was typically 1–5% and the percent difference between the TIR channels not strongly affected by the atmosphere was typically less than 0.5%. These results indicate the MASTER instrument should provide a well-calibrated instrument for Earth Science Studies. It should prove particularly valuable for those studies that leverage information across the electromagnetic spectrum from the visible to the TIR. © 2001 Elsevier Science Inc. All rights reserved.

1. Introduction

The MODIS/ASTER Airborne Simulator (MASTER) was developed to support scientific studies by the Advanced Spaceborne Thermal Emission and Reflection Radiometer (ASTER) and Moderate Resolution Imaging Spectroradiometer (MODIS) projects. ASTER and MODIS (Barnes, Pagano, & Salomonson, 1998; Salomonson, Barnes, Maymon, Montgomery, & Ostrow, 1989; Yamaguchi, Kahle, Tsu, Kawakami, & Pniel, 1998) are both spaceborne imaging instruments on the first Earth Observing System platform launched in the fall of 1999. The characteristics of these instruments are summarized in Table 1 and the characteristics of the MASTER instrument are summarized in Table 2.

The primary mission of MASTER is to:

Collect ASTER-like and MODIS-like data sets to support the validation of the ASTER and MODIS geophysical retrieval algorithms.

Collect these data sets at a higher spatial resolution than the spaceborne datasets to permit scaling studies and comparisons with in-situ measurements.

Underfly the Terra ASTER and MODIS sensors to provide an additional radiometric calibration to assist with satellite instrument performance characterization. This is particularly important for ASTER where on-board calibration is dependent on a single blackbody in the thermal infrared (TIR) and only partial aperture illumination in the visible–near infrared (VNIR).

---

* Corresponding author.
E-mail address: simon.j.hook@jpl.nasa.gov (S.J. Hook).

Table 1
Summary characteristics of the ASTER and MODIS instruments (modified from Kaufman, Herring, Ranson, & Collatz, 1999)

Instrument	ASTER	MODIS
Spatial resolution at nadir	15 m (4 channels-VNIR),	250 m (2 channels),
	30 m (5 channels-SWIR),	500 m (5 channels),
	90 m (5 channels-TIR)	1000 m (29 channels
Number of channels	14 channels	36 channels
Spectral range	0.5–12 μm	0.4–14 μm
Swath width	60 km	2330 km
Repeatability	Nominally 16 days[a]	Daily except near the equator
Stereo capability	Yes	No
Main measurements	General studies at the local scale	General land, ocean, and atmospheric
	(requiring high spatial resolution imagery)	global studies across the visible to
	across the visible to TIR spectrum	TIR spectrum

[a] Repeat coverage is possible at greater frequency for the visible–near infrared channels by instrument pointing. VNIR — visible near infrared. SWIR — shortwave infrared. TIR — thermal infrared.

A secondary mission of MASTER is to:

Provide a back-up instrument for the current MODIS Airborne Simulator (MAS), which is committed to a program of atmospheric and oceanic measurements (King et al., 1996).

Provide a wider spectral and dynamic range alternative to the Thermal Infrared Multispectral Scanner (TIMS, Palluconi & Meeks, 1985) for local-scale studies.

In order to meet these objectives the MASTER instrument must be well calibrated. Further, the calibration needs to be verified in-flight since the operating environment is very different to the laboratory calibration environment. Therefore, a validation experiment was conducted to characterize the performance of the instrument in-flight.

The MASTER instrument and data reduction procedures are described below followed by the results from a recent in-flight validation experiment. Finally, the results are summarized and conclusions drawn.

2. Instrument description

The MASTER instrument was developed by the NASA Ames Research Center in conjunction with the Jet Propulsion Laboratory. The instrument consists of three key components: the scanning spectrometer, the digitizer, and the storage system. The scanning unit was built by Sensys Technology (formerly Daedalus Enterprises), and the digitizer was a collaborative effort between Berkeley Camera Engineering and the Ames Airborne Sensor Facility (ASF) The data storage system and overall system integration were also provided by the ASF.

The MASTER instrument is similar to the MAS developed by the MODIS project (King et al., 1996). However, its has two key differences. First, MASTER supports a variety of scan speeds allowing it to acquire contiguous imagery from a variety of altitudes with differing pixel sizes (Table 2). Second, the channel posi-

tions are configured to more closely match those of ASTER and MODIS (Tables 3 and 4). However, the exact bandpasses of MASTER differ in detail from the filter-based ASTER and MODIS instruments. The system itself consists of a scanhead unit and a set of electronic subsystems, weighing 174 and 121 lb, respectively. The scanhead occupies 3.9 ft^3 of space, and the electronics utilize approximately 30 in. of vertical space in a standard 19 in. mounting rack.

The optical system is composed of a spectrometer mounted on a scanning fore-optic unit. Both the spectrometer and fore-optics portions are mated to an optical baseplate. The fore-optics consist of a full-face rotating scan mirror, canted 45° to the flight direction, directing light into an afocal Gregorian telescope with a 15.2-cm paraboloid main mirror. A folding mirror then directs the energy

Table 2
Summary characteristics of the MASTER instrument

Wavelength range	0.4–13 μm
Number of channels	50
Number of pixels	716
Instantaneous field of view	2.5 mrad
Total field of view	85.92°
Platforms	DOE King Air Beachcraft B200, NASA ER-2, and NASA DC-8
Pixel size DC-8	10–30 m
Pixel size ER-2	50 m
Pixel size B200	5–25 m
ER-2 range (without refueling)	3700 statute miles
B200 range (without refueling)	700 statute miles
DC-8 range (without refueling)	5403 statute miles
Scan speeds	6.25/12.5/25 rps
Products	Radiance at sensor (Level 1B)
Calibration VIS-SWIR	Laboratory Integrating Sphere
Calibration MIR-TIR	2 on-board blackbodies
Data Format	Hierarchical Data Format (HDF)
Digitization	16-bit

Table 3
Spectral characteristics of the visible–shortwave infrared MASTER channels

Channel	Full width half maximum	Channel center	Channel peak
1	0.0433	0.4574	0.458
2	0.0426	0.4981	0.496
3	0.0427	0.54	0.538
4	0.0407	0.5807	0.58
5	0.0585	0.6599	0.652
6	0.042	0.711	0.71
7	0.0418	0.7499	0.75
8	0.042	0.8	0.8
9	0.0417	0.8658	0.866
10	0.0407	0.9057	0.906
11	0.0403	0.9452	0.946
12	0.0542	1.6092	1.608
13	0.0526	1.6645	1.666
14	0.0514	1.7196	1.718
15	0.0521	1.7748	1.774
16	0.0506	1.8281	1.826
17	0.0457	1.8751	1.874
18	0.0575	1.9244	1.924
19	0.0504	1.9807	1.98
20	0.0481	2.0806	2.08
21	0.0511	2.1599	2.16
22	0.0508	2.2106	2.212
23	0.0513	2.2581	2.258
24	0.0683	2.3284	2.32
25	0.0641	2.3939	2.388

It should be noted the channel positions shift slightly between calibrations and therefore the calibration nearest the acquisition date should be used.

through a field stop aperture, and onto a 2.5-cm paraboloid Pfund assembly, which forms a collimated beam with a 2.5-mrad equivalent field of view. This is then directed by a deviating mirror into the spectrometer unit through a hole in the baseplate (Fig. 1). The spectrometer is divided into four output sections or ports, each with its own detector array and associated optics. The input energy is wavelength-separated by a chain of dichroic beam splitters, and directed into each of the four output ports of the spectrometer (Visible near infrared (VNIR), shortwave infrared (SWIR), mid-infrared (MIR) and Thermal infrared (TIR)). A diffraction grating is mounted at each output port, which spectrally disperses the energy through a lens and onto a linear detector array. The bandpass of each individual channel is determined by the geometry of the detector array and its location with respect to the grating. Three of the four detector arrays (two InSb and one HgCdTe) are cryogenically cooled with liquid nitrogen; the silicon array for the VNIR channels is temperature-stabilized with a thermal–electric cooler. The HgCdTe array used with the TIR channels also has a cooled linear-variable filter mounted over it to reduce background noise (a similar installation will be made on the MIR array of MASTER shortly). This grating-based design maximizes optical efficiency, while remaining radiometrically flat to within 1% across the total field of view, and is not spectrally dependent on viewing angle.

The analog electrical signals from each detector are passed through a series of low-noise preamplifiers on the scanhead, and are then passed to a digitizer via shielded twisted-pair cables. The first-stage preamplifiers on the Port 2 and 3 detector arrays (SWIR and MIR) are cryogenically cooled within the Dewar assemblies, to minimize noise. Specially designed adaptive, 16-bit analog-to-digital (A/D) converters are used in the digitizer, that actively track the DC level of the signal from the cooled detectors. This level, especially from HgCdTe arrays, typically drifts with time, and has been an historic source of calibration error in IR systems. The use of an actively adjusted, programmable preamplifier on the front end of the A/D converter allows this to be nullified, and the signal digitized very accurately, while preserving a full 16-bit dynamic range. Optical isolation was used, together with other noise reducing techniques, wherever possible in the system design. The digitized video signal is then merged with ancillary engineering and external navigation data, and is then stored on the hard disk. Further details of the optical system are given in King et al. (1996).

The MASTER channels are calibrated spectrally and radiometrically in the laboratory preflight and postflight. A preflight and postflight calibration is typically undertaken after major campaigns or periodically throughout the flight season. The MIR and TIR channels (26–50) are also radiometrically calibrated in-flight by viewing an internal

Table 4
Spectral characteristics of the mid-TIR MASTER channels

Channel	Full width half maximum	Channel center	Channel peak
26	0.1559	3.1477	3.142
27	0.1459	3.2992	3.292
28	0.1478	3.4538	3.452
29	0.1544	3.6088	3.607
30	0.1345	3.7507	3.757
31	0.1524	3.9134	3.912
32	0.1548	4.0677	4.067
33	0.153	4.2286	4.224
34	0.153	4.3786	4.374
35	0.1446	4.5202	4.522
36	0.1608	4.6684	4.667
37	0.1521	4.8233	4.822
38	0.1487	4.9672	4.962
39	0.1495	5.116	5.117
40	0.1578	5.2629	5.272
41	0.3645	7.7599	7.815
42	0.4333	8.1677	8.185
43	0.3543	8.6324	8.665
44	0.4253	9.0944	9.104
45	0.4083	9.7004	9.706
46	0.3963	10.116	10.115
47	0.5903	10.6331	10.554
48	0.6518	11.3293	11.365
49	0.4929	12.117	12.097
50	0.4618	12.8779	12.876

It should be noted the channel positions shift slightly between calibrations and therefore the calibration nearest the acquisition date should be used.
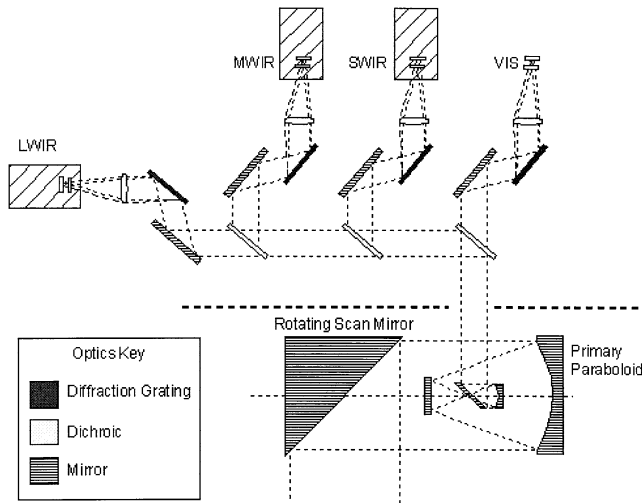
Fig. 1. MASTER optical layout.

hot and cold blackbody with each scanline. Because the MASTER system design is optically and mechanically identical to the MAS, the same laboratory calibration procedures are used (Arnold et al., 1996). Briefly, a 30-in. diameter integrating sphere is used as the primary radiometric source for calibrating the visible–shortwave infrared channels (1–25). The sphere is operated at four decreasing lamp levels, to establish linearity of the system response. The sphere itself is periodically calibrated against a NIST standard lamp, both by a team from the Goddard Space Flight Center and by the Ames Sensor Facility. Both the 30-in. sphere and the standard lamp/plaque assembly used as a primary source were also measured independently by NIST and the Univ. of Arizona Optical Sciences Dept. on Sept. 1–2, 1999. These measurements agreed within 5% with the working values currently being used for MASTER calibration (Butler, 2000). Spectral characterizations are preformed with both a scanning monochromter, and Fourier transform interferometer. This involves mounting the scanner over an 8-in. diameter collimator, interfaced to an optical bench for these measurements. This procedure is described in Arnold et al. (1996). The measured spectral response functions for some channels are atmospherically corrected with a radiative transfer model (MODTRAN), to remove the effects of water vapor and CO_2 absorption. Essentially, channels that have strong absorbers even over short path lengths. Spatial characterization and polarization sensitivity measurements of the instrument will be made at a future date. MASTER is also periodically characterized in a cold-chamber, to monitor radiometric and spectral stability at the operating temperature of the high altitude ER-2 aircraft.

The radiometric calibration of the MASTER instrument is also validated in-flight. Currently, plans call for the MASTER instrument to be flown on three aircraft. These are the Department of Energy (DOE) King Air Beachcraft B200, the NASA DC-8 and the NASA ER-2. Since each instrument has a unique operating environment it is neces-

sary to conduct a validation experiment on each platform. The validation of MASTER on the B200 platform is described herein. MASTER can acquire data with pixel sizes in the range of 5–25 m from this platform depending on surface and flight altitude. It should be noted that a custom air-fence was installed on the B200 to minimize calibration errors due to wind-blast over the exposed reference blackbodies. This phenomenon, first observed with the TIMS instrument flying on the NASA C-130 aircraft, produces a differential cooling on the surface of the blackbody that makes it impossible to accurately measure its temperature (Schmugge, Becker, & Li, 1991). A properly sized air-fence, installed forward of the scanner viewing aperture, minimizes turbulent airflow over these surfaces. Empirical data show that this greatly increases the calibration accuracy of the IR channels.

MASTER data are typically supplied as a standard product through the NASA Distributed Active Archive Center (DAAC) system, as a Level-1B product. This includes image data calibrated to radiance-at-sensor, together with ancillary files containing geo-location, navigation, and calibration data. The files are encapsulated in Hierarchical Data Format (HDF), for which several public domain viewers are available.

A quicklook is generated for each flightline and posted on the MASTER web site (http://masterweb.jpl.nasa.gov). Users can browse the on-line archive and order data at a nominal cost.

3. Ivanpah Playa, California

Ivanpah Playa is a dry lakebed on the border between California and Nevada. Interstate 15 traverses through the playa that is located about 50 km southwest of Las Vegas and is at an elevation of approximately 800 m. A 60×60 m area of the playa was selected as the test site (Fig. 2A). The size of the site gives approximately a 20×20 pixel area for the lowest altitude of the MASTER overflight and nearly a 5×5 pixel area for the high altitude pass of the B-200. This gives a reasonable number of pixels in the imagery while allowing rapid measurement of the surface reflectance with adequate sampling to understand the spatial heterogeneity of the test site. Tarpaulins were placed at one corner of the site to indicate its location in the MASTER imagery. The local atmosphere was characterized using a Reagan Sun Photometer and the surface reflectance was measured using an Analytic Spectral Devices FieldSpec FR.

The atmospheric characterization is based on solar extinction measurements and these data are converted to spectral optical depths that are used to describe aerosol parameters and columnar amounts of gaseous absorbers. The solar radiometer was calibrated in intercept to a precision of better than 1% in all bands. This leads to an optical depth retrieval better than 5% giving less than 0.2% uncertainty in the at-sensor radiance based on runs of the radiative
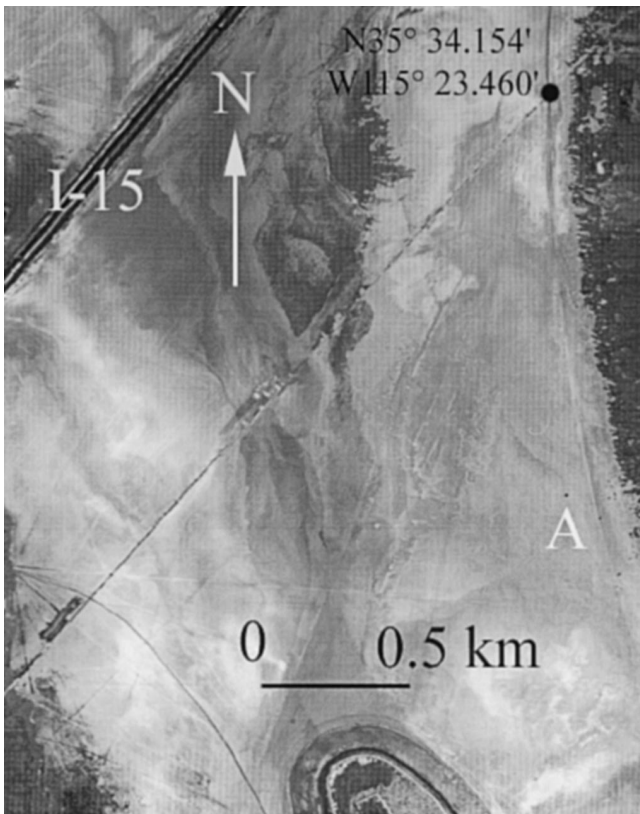
Fig. 2. MASTER image of the Ivanpah Playa site using data from Channel 6 (0.711 μm). Tarpaulin marking test site is just visible above the apex of the letter A.

transfer code (RTC). Fig. 3 shows the spectral optical thickness as a function of time for the day of the MASTER overflight for spectral bands centered at 441 and 781 nm. Molecular scattering optical thicknesses based on the atmospheric pressure have been removed from these results. Thus, the optical thicknesses shown in the figure are those due to aerosol scattering and absorption and a small amount of ozone absorption. As can be seen in the figure, the optical thickness shows a significant decrease early in the morning with an apparent leveling around 11 a.m. local standard time. Unfortunately, optical thickness data are not available for the actual overflight times and the optical thicknesses used to retrieve the aerosol size distribution were based on a 20-min average of data at the end of the collection. The lack of solar extinction measurements at the exact time of sensor overpass are not expected to be a significant source of uncertainty due to the high surface reflectance of the test site and low aerosol loading. To evaluate this effect, the aerosol optical thickness was doubled and the radiances at the sensor recomputed. This led to less than 0.7% change in radiance with the effect becoming smaller at longer wavelengths. For the Ivanpah test site, this level of change in optical thickness has not been seen without significant amounts of blowing dust due to high-wind conditions. Since this was not the case for this date, the effects of missing solar extinction data is not a significant source of uncer-

tainty. Additional effects due to missing data at overpass are incorrect values for the aerosol size distribution and column ozone. Changing the Junge parameter by 20% (a 0.7 change in Junge parameter), led to less than 0.2% changes in the radiance. Assuming an uncertainty in ozone amount of 25% led to significant changes in only bands 2 and 3 with 2% and 3% changes, respectively. Thus, the overall uncertainty in these bands would be greater than those of bands with no ozone absorption.

The reflectance of the surface was measured using an Analytic Spectral Devices FieldSpec FR. This instrument covers the wavelength range of 350–2500 nm with output reported at 1 nm intervals. It uses three separate gratings to cover this spectral range. The first grating covers approximately the range from 350 to 1000 nm at better than 1 nm spectral resolution. The second and third gratings cover the 1000 to 2000 nm and 2000 to 2500 nm spectral ranges, respectively, at 10 nm resolution. Measurements of the surface were made by transporting the FieldSpec across the test site and measuring upwelling radiance. The upwelling radiance is converted to reflectance by comparing the radiance to that from a panel of known reflectance. The reference for this work was a 46 cm^2 monolithic piece of Spectralon. The 60×60 m test site was divided into eight east–west sections. Forty sample spectra were collected within each section with each sample consisting of an average of 30 individual spectra. Measurements of the reflectance standard were made every 160 samples. These reference measurements are corrected for the bidirectional reflectance effects of the reference panel and for changing sun angle during the 30-min measurement period (Biggar et al., 1998). Because atmospheric conditions were relatively stable during the 30-min data collection, no correction is made for changing diffuse sky illumination.
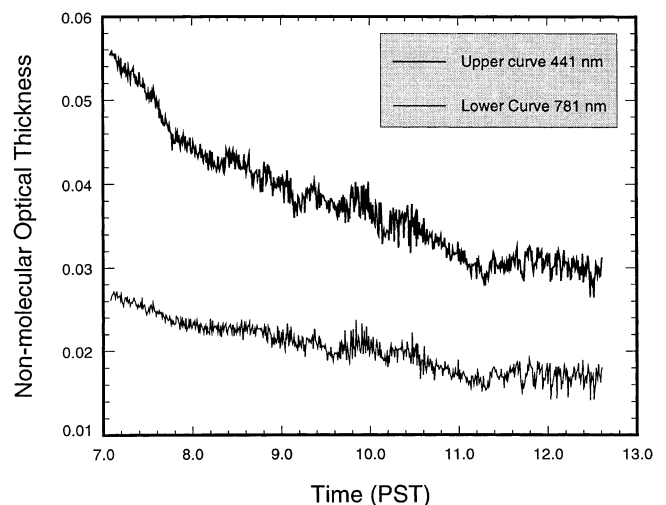

Fig. 3. Spectral optical thickness as a function of time for the day of the MASTER overflight for spectral bands centered at 441 and 781 nm. Molecular scattering optical thicknesses based on the atmospheric pressure have been removed from these results.
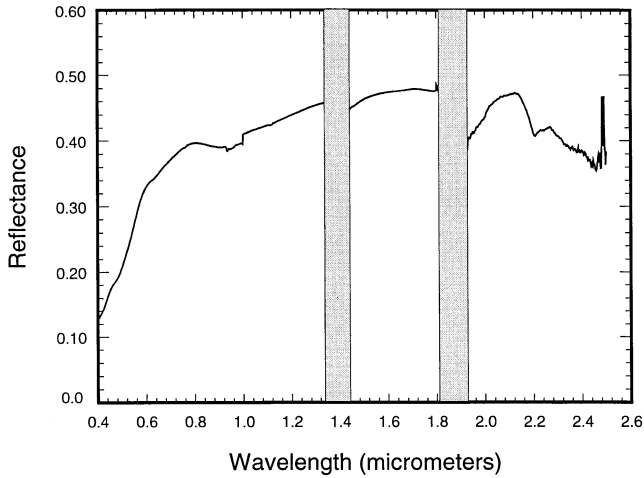
Fig. 4. Surface reflectance of Ivanpah Playa measured with the Analytical Spectral Devices FieldSpec FR spectrometer. The atmospheric water bands (noise dominated) around 1.4 and 1.9 μm have been masked out. Obvious artifacts are apparent in the spectrum around 1.0 μm and beyond 2.4 μm.

A total of three sets of reflectance data were collected between 11:00 and 12:30 local standard time. Fig. 4 shows the retrieved reflectance based on the average of the 320 samples from the test site for the data collected between 12:00 and 12:30. The standard deviation of the average of the data shown is less than 0.005 throughout the spectrum corresponding to a percent standard deviation of about 1%
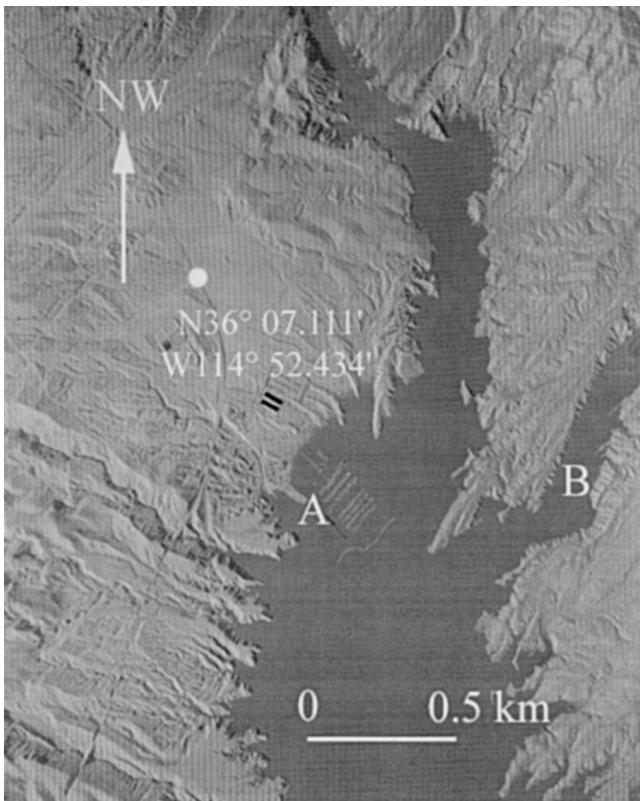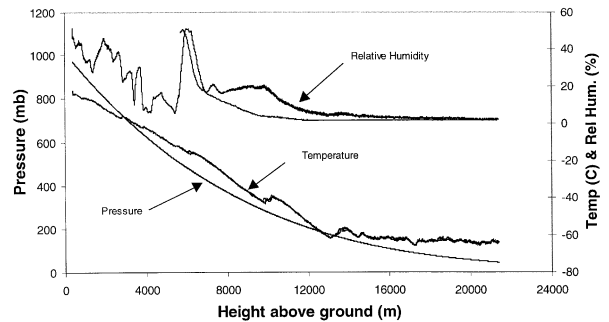
for much of the spectrum. Similar results, both magnitude and variability, were obtained for the earlier two data collections with all three sets agreeing to better than 1.5% of the reflectance.

4. Lake Mead, Nevada

Lake Mead is located northeast of Las Vegas, NV. Measurements were made at two localities at Lake Mead. The first locality was the end of a peninsula slightly east of the Las Vegas Bay Marina (Fig. 5, Locality A). This site was used to launch the atmospheric sounding balloon. The second locality was Gypsum Bay (Fig. 5, Locality B) where the radiative surface temperature and bulk water temperature was measured by radiometers and buoy-mounted tempera-ture loggers, respectively.

Fig. 6 illustrates the atmospheric profiles of pressure, temperature, and relative humidity obtained from the launch of an atmospheric sounding balloon at 12 noon. The sounder ascended to approximately 20 km at which point the balloon burst and the sensor package continued to transmit on the descent until contact was lost with the receiver at approximately 5 km. It is clear that the bulk of the variation in water vapor occurs below 5 km (Fig. 6A).

12-2-98 Sounder and MODTRAN Profile

Fig. 5. MASTER image of the Lake Mead site using data from Channel 42 (8.185 μm). Images labels: A — Las Vegas Bay Marina; B — Gypsum Bay.
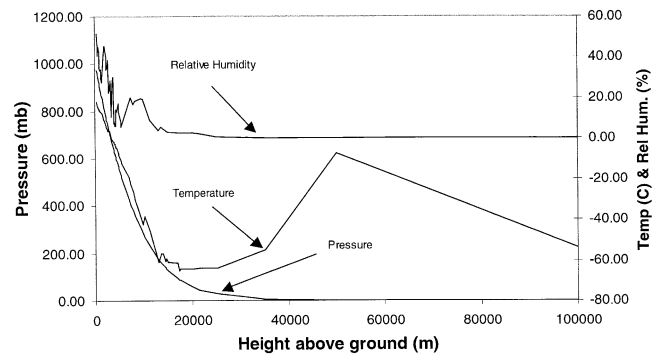
Fig. 6. Atmospheric profiles of pressure, temperature and relative humidity obtained from the launch of an atmospheric sounding balloon at 12 noon. (a) Profiles from 0–24 km; (b) Profiles from 0–100 km. The relative humidity device froze at 5.8 km, producing a spike. A point was taken on either side of the spike and then points were taken until 20 km above which the default mid-latitude profile from MODTRAN was used.
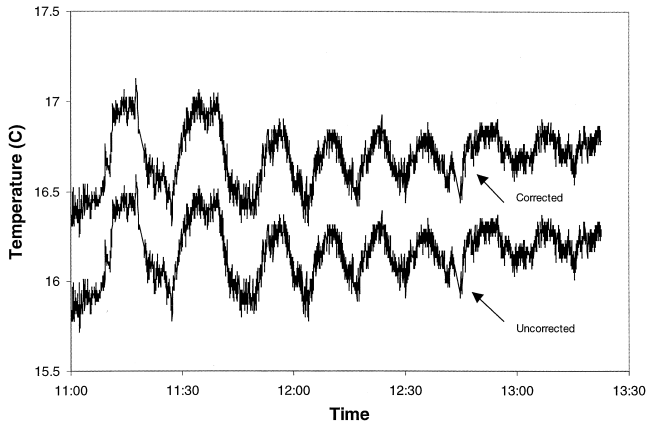
Fig. 7. Surface brightness temperature and surface kinetic temperature for Gypsum Bay from one of the JPL self-calibrating radiometers mounted on either side of a pontoon boat.

At 5.8 km there is a spike in the relative humidity, this spike is an artifact caused by freezing of the relative humidity device (Fig. 6A). The sounder data were used to create an input profile for use with the MODTRAN RTC to predict the radiance at sensor from the surface radiance measurements. The values in the profile above 20 km were taken from the default mid-latitude winter model (Fig. 6B).

Fig. 7 illustrates the surface radiative temperature recovered from one of the two JPL self-calibrating radiometers mounted on either side of a pontoon boat. The lower curve is the surface brightness temperature and the upper curve is the surface kinetic temperature. The surface kinetic temperature is derived by correcting for surface emissivity and subtracting the sky radiance reflected by the surface into the path of the radiometer:

$$L_{sur} = \frac{L_{obs} - L_{path} - \tau(1 - \varepsilon)L_{down}}{\tau\varepsilon} \quad (1)$$

where: L_{sur} = surface radiance; L_{obs} = observed radiance; L_{path} = path radiance; τ = atmospheric transmission; ε = sursurface emmisivity; and L_{down} = downwelling atmospheric radiance.

The kinetic temperature is obtained from the surface radiance by inverting the Planck equation. The radiance terms are calculated by integrating over the system response curve for the JPL self-calibrating radiometer (Eq. (2)).

$$L_{\lambda} = \int_{\lambda} L(\lambda)R(\lambda)\partial\lambda \quad (2)$$

Eq. (1) is solved iteratively. The sky radiance term is obtained from the RTC driven by the profile illustrated in Fig. 6. The emissivity of the water was obtained from the ASTER spectral library. The JPL self-calibrating radiometer has internal hot and cold blackbodies and is NIST traceable. NIST traceability is provided by laboratory calibration of the radiometer against the JPL cone blackbody that was traced to NIST using their transfer radiometer (Kannenberg,

1998). Provided the internal blackbodies bracket the scene, the radiometer is accurate to ±0.2 K. The radiometer-derived surface temperatures are cyclic over time. This results from the boat traversing back and forth between the mouth and landward end of Gypsum Bay (Figs. 5 and 7). The first couple of traverses went closer to the land and further out of the bay and as a result have greater amplitude than the subsequent traverses. The radiometer measurements were made every second and the location of the boat at the time of the measurement was recorded by differential GPS, allowing the location of the boat at the time of the overpass to be determined. The differential GPS measurements are accurate to 1–2 m.

Fig. 8 illustrates the kinetic water temperature measured from a buoy-mounted temperature logger and self-calibrating radiometer. The loggers were calibrated in a NIST traceable water bath at the University of Davis. The buoy temperatures step compared to the radiometer data. The steps are due to the digitization interval for the temperature loggers. The radiometric or skin temperature is a few tenths of a degree cooler than the logger temperatures as expected due to wind-induced cooling of the surface.

5. Comparison of MASTER sensor radiance to field derived radiance

5.1. Visible–shortwave infrared

The radiance-validation work at Ivanpah Playa relies on the reflectance-based method, which has a proven history of use through the radiometric calibrations of Landsat-4 and -5 Thematic Mapper and SPOT-1, -2, and -3, the AVIRIS, and a Daedalus scanner (Balick, Golanics, Shines, Biggar, & Slater, 1991; Gellman et al., 1993; Slater et al., 1987; Thome, Gustafson-Bold, Slater, & Farrand, 1996; Vane et al., 1993). This approach uses ground-based measurements
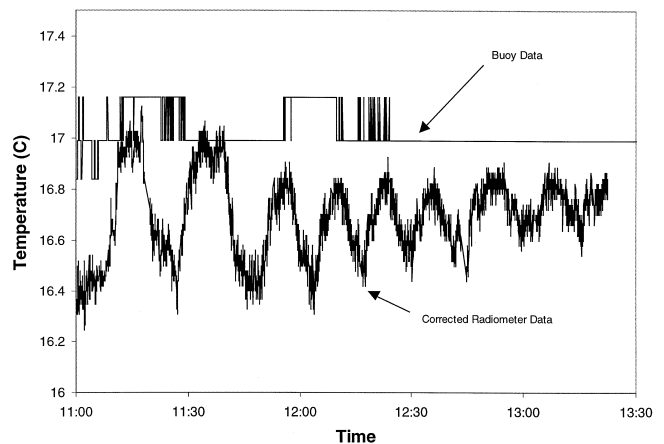

Fig. 8. Surface kinetic temperature of Gypsum Bay measured radiometer and bulk temperature measured by buoy-mounted temperature logger.

of the surface and atmosphere at a selected site to predict radiance at the top of the atmosphere.

The above results were used in a modified version of a Gauss–Seidel iteration RTC to predict the at-sensor radiances for each of the five runs at 1-nm intervals from 350–2500 nm (Herman & Browning, 1965; Thome et al., 1996). The RTC assumes the surface to be lambertian and homogeneous. Because of the low altitudes of the aircraft, high reflectance of the surface, and low aerosol loading, adjacency effects due to multiple scattering in the atmosphere will be minimal and the assumption of homogeneity will cause less uncertainty in the results than the uncertainty in the reflectance measurements. The assumption of a lambertian surface is also not a significant source of uncertainty since past measurements of the surface BRDF of this test site show the surface to be within 5% of lambertian out to 40°

view angles and the solar angle at the time of sensor overpass. Model runs of the RTC with historical BRDF data for the site give less than 0.5% uncertainty in the at-sensor radiances.

The atmospheric conditions used in the code are based on the results of the atmospheric measurements described above. The primary instrument used to characterize the atmosphere over the site is the solar radiometer. The solar radiometers are relatively calibrated immediately prior to, during, or after each field campaign. Data are used in a Langley method retrieval scheme to determine spectral atmospheric optical depths (Gellman, Biggar, Slater, & Bruegge, 1991). The optical depth results are used as part of an inversion scheme developed by the RSG to determine ozone optical depth and a Junge aerosol size distribution parameter (Biggar, Gellman, & Slater, 1990). The size distribution and columnar ozone are used to determine the

Table 5

Comparison of the predicted radiance at sensor with the measured radiance at sensor for the Ivanpah and Lake Mead sites

Channel number	Center wavelength	Radiances (W/m² μm sr)								
		Low altitude			Medium altitude			High altitude		
		Predict	MASTER	% difference	Predict	MASTER	% difference	Predict	MASTER	% difference
1	0.457	58.288	58.400	− 0.192	58.597	57.100	2.554	60.256	57.200	5.072
2	0.498	66.493	68.500	− 3.018	64.766	64.900	− 0.207	64.984	63.700	1.976
3	0.540	79.552	81.300	− 2.197	75.832	75.500	0.437	74.765	72.500	3.030
4	0.581	90.558	91.500	− 1.040	85.136	83.800	1.569	83.082	79.700	4.071
5	0.660	90.166	92.000	− 2.034	84.044	84.100	− 0.067	81.487	79.200	2.807
6	0.711	82.338	83.800	− 1.775	75.329	76.300	− 1.290	72.522	71.500	1.409
7	0.750	76.452	79.000	− 3.333	69.786	71.900	− 3.030	67.017	67.200	− 0.273
8	0.800	73.746	77.600	− 5.225	68.028	70.700	− 3.929	65.678	66.000	− 0.490
9	0.866	64.052	70.300	− 9.755	59.695	64.500	− 8.049	57.838	60.100	− 3.911
10	0.906	48.586	53.000	− 9.084	43.273	48.000	− 10.923	41.310	44.400	− 7.481
11	0.945	28.558	34.030	− 19.159	23.492	30.270	− 28.853	21.885	27.470	− 25.523
12	1.609	19.857	21.060	− 6.061	18.348	19.390	− 5.681	17.633	18.150	− 2.933
13	1.665	18.139	19.450	− 7.226	16.808	17.920	− 6.615	16.194	16.850	− 4.049
14	1.720	15.135	16.390	− 8.290	13.855	15.060	− 8.699	13.321	14.240	− 6.899
15	1.775	8.361	9.440	− 12.911	7.190	8.580	− 19.332	6.795	8.090	− 19.058
16	1.828	0.496	1.500	− 202.358	0.350	1.400	− 300.114	0.313	1.200	− 283.264
17	1.875	0.035	0.730	− 1973.864	0.030	0.690	− 2238.983	0.028	0.570	− 1943.011
18	1.924	0.299	1.100	− 267.401	0.180	0.970	− 440.390	0.147	0.790	− 436.320
19	1.981	3.545	3.800	− 7.196	2.687	3.320	− 23.581	2.390	3.020	− 26.365
20	2.081	6.923	7.140	− 3.134	5.975	6.410	− 7.288	5.541	5.950	− 7.391
21	2.160	6.673	7.210	− 8.055	6.143	6.600	− 7.436	5.913	6.250	− 5.698
22	2.211	5.686	6.340	− 11.506	5.213	5.780	− 10.875	4.999	5.430	− 8.626
23	2.258	5.277	5.600	− 6.127	4.798	5.090	− 6.088	4.554	4.780	− 4.958
24	2.328	4.021	3.990	0.781	3.535	3.580	− 1.267	3.296	3.360	− 1.936
25	2.394	2.455	2.520	− 2.643	2.045	2.250	− 10.041	1.885	2.100	− 11.418
41	7.760	6.193	6.182	0.187	5.583	5.547	− 1.040	5.101	4.881	4.325
42	8.168	7.163	7.155	0.117	6.967	6.899	− 0.050	6.844	6.763	1.186
43	8.632	7.681	7.701	− 0.258	7.613	7.563	− 0.226	7.588	7.559	0.379
44	9.094	7.975	7.990	− 0.181	7.930	7.900	− 0.251	7.916	7.874	0.520
45	9.700	8.175	8.211	− 0.441	8.102	8.039	0.027	8.023	8.002	0.262
46	10.116	8.223	8.253	− 0.362	8.199	8.165	− 0.017	8.189	8.151	0.462
47	10.633	8.156	8.196	− 0.483	8.133	8.107	− 0.574	8.130	8.092	0.470
48	11.329	7.931	7.952	− 0.255	7.911	7.879	− 0.108	7.915	7.880	0.447
49	12.117	7.525	7.541	− 0.217	7.493	7.458	− 1.422	7.490	7.440	0.670
50	12.878	7.040	7.011	0.408	6.956	6.854	− 1.784	6.910	6.871	0.556

The TIR image values were obtained from averages of 9 × 9, 6 × 6, and 3 × 3 pixel blocks for the low, medium, and high lines, respectively. No data are provided for the mid-infrared channels due to the low signal to noise of MASTER in this region.

optical depths at 1-nm intervals from 350 to 2500 nm. Columnar water vapor is derived using a modified Langley approach and comparisons to radiosonde balloon results shows better than 10% agreement using this approach (Thome, Herman, & Reagan, 1992). The retrieved columnar water vapor is used as an input to MODTRAN3 to determine transmittance for the sun-to-surface-to-satellite path for 1-nm intervals from 350 to 2500 nm.

The proper solar zenith angle is used for each altitude run, and we include effects due to sensor altitude. The view angle used for the radiative transfer calculations is based on the location of the test site relative to the nadir point in the image and the swath width of the sensor. The output of the RTC is relative radiance that is converted to absolute radiance using MODTRAN3 derived solar irradiance interpolated to 1-nm increments and corrected for the appropriate earth–sun distance. These 1-nm absolute radiances are band-averaged using the MASTER spectral response curves for each band in the solar reflective.

The band-averaged radiances from the radiative transfer calculations are compared to radiances derived from the MASTER data. This was done by first locating the test site in the image based on the tarpaulins placed at two corners of the site. All pixels in the area within the tarpaulin are used to determine the average radiance and this is done for all three altitude runs. As an indication of the site's homogeneity, the standard deviation of the average is < 1% for bands with little atmospheric absorption. To estimate the uncertainty due to a misregistration between the reflectance data and the MASTER data, the test site in the MASTER image was shifted by up to 2 pixels and recomputed. The results of these tests indicate that registration uncertainties are less than 0.2% in all solar-reflective bands with little atmospheric absorption.

5.2. Thermal infrared

After calibration the MASTER at-sensor TIR radiance (Ls) for a given wavelength (λ) can be written as:

$$Ls_\lambda = \left[\varepsilon_\lambda L_{bb\lambda}(T) + (1 - \varepsilon_\lambda)L_{sky\lambda}\right]\tau_\lambda + L_{atm\lambda} \qquad (3)$$

where: ε_λ = surface emissivity at wavelength λ; $L_{bb\lambda}(T)$ = spectral radiance from a blackbody at surface temperature T; $L_{sky\lambda}$ = sky radiance (spectral downwelling radiance incident upon the surface from the atmosphere); τ_λ = transmittance (spectral atmospheric transmission); and $L_{atm\lambda}$ = path radiance (spectral upwelling radiance from atmospheric emission and scattering that reaches the sensor).

Eq. (3) was used to predict the radiance at-sensor, which was convolved with the MASTER system response function using Eq. (4).

$$L_\lambda = \frac{\int_{\lambda_1}^{\lambda_2} \Psi(\lambda)\varepsilon_\lambda L_{BB}(\lambda, T)d\lambda}{\int_{\lambda_1}^{\lambda_2} \Psi(\lambda)d\lambda} \qquad (4)$$

where Ψ is the sensor response function and λ_1 and λ_2 are the lower and upper boundaries of each channel.

The atmospheric terms in Eq. (3) were obtained from a radiative transfer model (MODTRAN 3.5, Berk, Bernstein, & Robertson, 1989) driven by the local atmospheric data.

6. Discussion

Table 5 shows the MASTER radiance, the predicted radiance, and the percent difference between the two radiances for the three overpasses. The percent difference between the channels not strongly affected by the atmosphere in the visible–shortwave infrared is typically 1–5% and the percent difference between the TIR channels not strongly affected by the atmosphere is typically less than 0.5% (< 0.3 K). In the TIR there does not appear to be a systematic discrepancy between the data from the three flight altitudes, suggesting the TIR channels are not strongly affected by wind-blast as was observed in earlier similar experiments prior to the installation of the airfence. The percent difference in channels strongly affected by atmospheric absorption is very large, such as those around the 0.94 and 1.8 μm water absorption bands, due to the low signal at these wavelengths. The large percent difference in Channel 22 is probably due to surface variability. Channel 22 is centered on 2.2 μm where the playa has a strong absorption caused by the presence of hydroxyl-bearing (clay) minerals. In the TIR channels the percent difference is slightly larger at the shortest and longest wavelengths due to water and CO_2 absorption, respectively. Due to the low signal to noise of the MASTER MIR channels the instrument was not radiometrically validated in this wavelength region. Plans are underway to add a linear variable filter to the MIR channels to improve the signal to noise at which time these channels will be radiometrically validated in-flight.

7. Summary and conclusions

A new multispectral scanner, termed MASTER, has been developed to simulate and validate data from the ASTER and MODIS satellite instruments. The scanner acquires data over the spectral range 0.4 to 13 μm in 50 spectral channels at a variety of spatial resolutions. Results from an in-flight validation experiment indicate the instrument is well calibrated over the range of conditions utilized in this study. Several data sets have been acquired with MASTER (including the data from this study) and are available for browsing and ordering from: http://masterweb.jpl.nasa.gov.

It is anticipated the instrument will prove especially valuable for studies that leverage data over the full spectral range at high spatial resolution since such information is not currently available from other airborne instruments.

Acknowledgments

The research described in this paper was carried out in part at the Jet Propulsion Laboratory, California Institute of Technology, under a contract with the National Aeronautics and Space Administration as part of the Earth Observing System Mission to Planet Earth Program.

Numerous people have contributed to the validation effort for the MASTER instrument. In particular we would like to thank Ali Abtahi, Ron E. Alley, Timothy Thompson, and Degu Gu from the Jet Propulsion Laboratory, and Stuart F. Biggar, John L. Lamarr, Brian I. Magi, and Marek Mienko from the University of Arizona.

We would also like to acknowledge the invaluable support of the MASTER instrument engineering team at NASA Ames Research Center, in particular Edward Hildum, Patrick Grant, Pavel Hajek, and Jeannette van den Bosch.

Reference herein to any specific commercial product, process, or service by trade names, trademark, manufacturer or otherwise does not imply endorsement by the United States or the Jet Propulsion Laboratory, California Institute of Technology.

References

Arnold, G. T., Fitzgerald, M. F., Grant, P. S., Platnick, S., Tsay, S., Myers, J. S., & King, M. D. (1996). MODIS Airborne Simulator Radiometric Calibration. *SPIE Proceedings, Earth Observing System Conference, 2820*, 56–66.

Balick, L. K., Golanics, C. J., Shines, J. E., Biggar, S. F., & Slater, P. N. (1991). The in-flight calibration of a helicopter-mounted Daedalus multispectral scanner. *Proceedings of SPIE, 1493*, 215–223.

Barnes, W. L., Pagano, T. S., & Salomonson, V. V. (1998). Pre-launch characteristics of the Moderate Resolution Imaging Spectroradiometer (MODIS) on EOS AM1. *Transactions on Geoscience and Remote Sensing, 36*, 1088–1100.

Berk, A., Bernstein L. S., & Robertson, D.C. (1989). MODTRAN: a moderate resolution model for LOWTRAN 7. Tech. Rep. GL-TR-89-0122, Geophys. Lab., Bedford, MA.

Biggar, S. F., Gellman, D. I., & Slater, P. N. (1990). Improved evaluation of optical depth components from Langley plot data. *Remote Sensing of the Environment, 32*, 91–101.

Biggar, S. F., Labed, J., Santer, R. P., Slater, P. N., Jackson, R. D., & Moran, M. S. (1998). Laboratory calibration of field reflectance panels. *Proceedings of SPIE, 924*, 232–240.

Butler, J. (2000). Personal communication of MODIS Airborne Simulator Annual Meeting Notes. Goddard Space Flight Center, March 2000.

Gellman, D. I., Biggar, S. F., Dinguirard, M. C., Henry, P. J., Moran, M. S., Thome, K. J., & Slater, P. N. (1993). Review of SPOT-1 and-2 calibrations at White Sands from launch to present. *Proceedings of SPIE, 1938*, 118–125.

Gellman, D. I., Biggar, S. F., Slater, P. N., & Bruegge, C. J. (1991). Calibrated intercepts for solar radiometers used in remote sensor calibration. *Proceedings of SPIE, 1493*, 175–180.

Herman, B. M., & Browning, S. R. (1965). A numerical solution to the equation of radiative transfer. *Journal of the Atmospheric Sciences, 22*, 559–566.

Kannenberg, B. (1998). IR instrument comparison workshop at the Rosenstiel School of Marine and Atmospheric Science (RSMAS). *Earth Observer, 10*, 38–42.

Kaufman, Y. J., Herring, D. D., Ranson, K. J., & Collatz, G. J. (1999). Earth observing system AM1 mission to earth. *IEEE Transactions on Geoscience and Remote Sensing, 36*, 1045–1055.

King, M. D., Menzel, W. P., Grant, P. S., Myers, J. S., Arnold, G. T., Platnick, S. E., Gumley, L. E., Tsay, S. C., Moeller, C. C., Fitzgerald, M., Brown, K. S., & Osterwisch, F. G. (1996). Airborne scanning spectrometer for remote sensing of cloud, aerosol, water vapor and surface properties. *Journal of Atmospheric and Oceanic Technology, 13*, 777–794.

Palluconi, F. D., & Meeks, G. R. (1985). Thermal infrared multispectral scanner (TIMS): an investigator's guide to TIMS data. *JPL Publication, 85-32*.

Salomonson, V. V., Barnes, W. L., Maymon, P. W., Montgomery, H. E., & Ostrow, H. (1989). MODIS: advanced facility instrument for studies of the earth as a system. *IEEE Transactions on Geoscience and Remote Sensing, 27*, 145–153.

Schmugge, T. J., Becker, F., & Li, Z.-L. (1991). Spectral emissivity variations observed in airborne surface temperature measurements. *Remote Sensing of the Environment, 35*, 95–104.

Slater, P. N., Biggar, S. F., Holm, R. G., Jackson, R. D., Mao, Y., Moran, M. S., Palmer, J. M., & Yuan, B. (1987). Reflectance- and radiance-based methods for the in-flight absolute calibration of multispectral sensors. *Remote Sensing of the Environment, 22*, 11–37.

Thome, K. J., Gellman, D. I., Parada, R. J., Biggar, S. F., Slater, P. N., & Moran, M. S. (1993). In-flight radiometric calibration of Landsat-5 Thematic Mapper from 1984 to present. *Proceedings of SPIE, 1938*, 126–130.

Thome, K. J., Gustafson-Bold, C. L., Slater, P. N., & Farrand, W. H. (1996). In-flight radiometric calibration of HYDICE using a reflectance-based approach. *Proceedings of SPIE, 2821*, 311–319.

Thome, K. J., Herman, B. M., & Reagan, J. A. (1992). Determination of precipitable water from solar transmission. *Journal of Applied Meteorology, 31*, 157–165.

Vane, G., Green, R. O., Chrien, T. G., Enmark, H. T., Hansen, E. G., & Porter, W. M. (1993). The Airborne Visible/Infrared Imaging Spectrometer (AVIRIS). *Remote Sensing of the Environment, 44*, 127–143.

Yamaguchi, Y., Kahle, A. B., Tsu, H., Kawakami, T., & Pniel, M. (1998). Overview of advanced spaceborne thermal emission reflectance radiometer. *IEEE Transactions on Geoscience and Remote Sensing, 36*, 1062–1071.